ARTICLE

In-situ biomimetic mineralization of microfluidic paper as fluorescent sensor for nitrite detection

Received 00th January 20xx,
Accepted 00th January 20xx

DOI: 10.1039/x0xx00000x

Isabel Blasco-Pascual,[a,c] Inmaculada Ortiz-Gómez,[a,c] Luis F. Capitán-Vallvey,[a,c] José M. Delgado-López,[b,c] Gloria B. Ramírez-Rodríguez,[b,c,*] and Alfonso Salinas-Castilloa[c,*]

Herein, a novel luminescent platform has been designed via in-situ mineralization of microfluidic paper-based analytical devices (µPAD) made of cellulose. The cellulose nanofibers were homogenously mineralized with terbium-doped calcium phosphate nanoparticles resulting in a luminescent composite material, which exhibits the characteristic green emission from Tb3+ ions, stable during long periods of time (6 months). This strong green emission is selectively quenched upon addition of nitrite due to the dynamic quenching of the emission, thus making the µPAD a potential sensor for the quantification of nitrite, a hazardous pollutant in water. This µPAD presents high sensitivity with detection limit (10 µM) lower than the permissible limits of nitrite in drinking water (65 µM) and it also displays good accuracy and reproducibility in real water samples. The biomimetic mineralization of µPAD in the presence of lanthanide ions holds promise for an environmentally friendly design of a rapid and efficient analytical method for monitoring of water pollutants and ensuring water quality, one of the biggest challenges of this century.

Introduction

Water pollution has become a serious worldwide problem due to their lethal, hazardous, and adverse effects on both the environment and human beings.[1] The population growth, urbanisation, industrialisation and extensive agriculture have contributed to the declined of water quality becoming water pollution prevention and control one of the main environmental objectives of the European Taxonomy Regulation (2020/852).[2] The widespread use of nitrogen fertilizer is one of the main causes of water pollution in Europe.[3] Nitrates and organic nitrogen compounds from fertilizer and manure enter groundwater through leaching and reach surface water through runoff from agricultural fields.[4] Nitrate reduces to nitrite, which together with nitrite from food preservative industries, has a great potential threat to human health. The excessive consumption of nitrite ions leads to the irreversible oxidation of hemoglobin to methemoglobin and the generation of carcinogenic N-nitrosamines.[4–6] The World Health Organization (WHO) has established the maximum contaminant level of nitrite ions in 3 ppm (65 µM) in drinking water.[7,5] The monitoring of NO_2^- in water resources is one of the global challenges that society must address in this century aiming to control water pollution and reduce adverse effects on both the environment and human beings.

The common spectroscopic methods for accurate and sensitive nitrite detection include UV-vis spectroscopy, chemiluminescence, chromatography, high-performance liquid chromatography, capillary electrophoresis and flow injection analysis.[8] Nevertheless, these methods have limitations such as the need of expensive instrumentation and sample pre-treatment, tedious detection procedures and being time-consuming.[8] Fluorescent sensors show the greatest potential to overcome these drawbacks due to their rapid and sensitive response, easy operation, low-cost and time savings.[1,9] Nonetheless, the low photochemical stability and inherent toxicity of current fluorescent sensors hamper its application in real scenario.[1,10,11] Hence, the design of analytical platforms for water monitoring that combine high sensitivity, selectivity, long-term stability and accuracy with low cost, portability and user friendliness is still in its infancy.[1,9]

The mineralization of biological tissues in living organism has been a source of inspiration to design sophisticated nanostructured hybrid materials with highly controllable and specialized properties.[12–15] This is a complex process controlled by an organic matrix that serves as a structural template controlling both the nucleation and subsequent crystal growth of the mineral phase, and thus playing a predominant role in the morphology and 3D distribution of the mineral within the organic matrix.[16] Bone mineralization has inspired the development of bio-inspired high-performance composite materials.[12–16] Cellulose mineralization inspired on bone formation has been explored to construct new and attractive hybrid materials with potential physicochemical and biological properties for biomedical and environmental applications including bone

---

[a] *Department of Analytical Chemistry, University of Granada, Faculty of Science, Av. Fuente Nueva, s/n, 18071 Granada, Spain*
[b] *Department of Inorganic Chemistry, University of Granada, Faculty of Science, Av. Fuente Nueva, s/n, 18071 Granada, Spain*
[c] *Unit of Excellence in Chemistry applied to Biomedicine and the Environment of the University of Granada, Spain*

† Footnotes relating to the title and/or authors should appear here.

Electronic Supplementary Information (ESI) available: [details of any supplementary information available should be included here]. See DOI: 10.1039/x0xx00000x regeneration, drug delivery, dental repair and the removal of environmental pollutants such as dyes, heavy metals (*i.e.* lead, cobalt) or antibiotics.[17–20] Bone mineralization has also inspired the synthesis of biocompatible and non-toxic phosphorescent nanoplatforms, based on the doping of calcium phosphate nanoparticles with lanthanide ions (*i.e.,* Eu^{3+}, Tb^{3+} or Nd^{3+}). These doped nanoparticles offer several advantages such as long luminescence lifetime, high quantum yield, sharp emission bands, colour tuning depending on the ions doped and good resistance to photobleaching from environmental cues.[21,22] Owing to these exceptional properties, these luminescent nanoparticles have potential applications in nanomedicine, specifically in diagnostics (imaging and biosensors) and theragnostics.[21,22] Eu- and Tb-doped hydroxyapatite nanowires have been embedded on a paper through a simple vacuum filtration toward developing a free-standing luminescent, fire-resistant and water-proof anticounterfeiting material.[23] In a recent work, luminescent terbium doped fluorapatite/agar nanocomposite synthesized via an environmentally friendly biomineralization process showed high selectivity and sensitivity for the detection for UO_2^{2+}, Cu^{2+}, and Cr^{3+} ions in water, becoming a potential luminescence sensor for environmental monitoring applications.[24]

This work is aimed at designing novel luminescent microfluidic paper-based analytical devices (µPADs) through bioinspired mineralization strategy in the presence of terbium ions.[25–27] We compared two methodologies: ex-situ *vs* in-situ mineralization of the detection area of the µPAD. The latter, which vastly improved the homogeneity of the as-synthesized hybrid material, was selected for the evaluation of the luminescent properties of the designed µPADs and its suitability as nitrite sensor for water monitoring.

Materials and methods

Chemicals and materials

Calcium chloride dihydrate ($CaCl_2 \cdot 2H_2O$, ≥ 99.0% pure), potassium citrate dihydrate ($K_3(C_6H_5O_7) \cdot 2H_2O$, ≥ 99.0% pure), potassium hydrogen phosphate (K_2HPO_4, ≥ 99.0% pure), potassium hydroxide (KOH, ≥ 90.0%), terbium (III) nitrate pentahydrate ($Tb(NO_3)_3 \cdot 5H_2O$, ≥ 99.9% pure) were purchased from Sigma Aldrich (Sigma-Aldrich Química S.A., Spain). All the solutions were prepared with ultrapure water (0.22 µS/cm, 25 °C, MilliQ©, Millipore). Filter paper (ref. 1240, basis weight 85 g/m^2, thickness 200 µm; retention 14-18 µm) from Filter-lab (Barcelona, Spain) was used to fabricate the microfluidic paper-based analytical device (µPAD).

Production of the microfluidic paper-based analytical device (µPAD)

The µPAD were designed using Illustrator software (Adobe Systems) and the design was exported as an FS file to the controller software of a desktop laser engraver wits a 12 W CO_2 laser source (Rayjet, www.rayjetlaser.com). For the production, a sheet of paper was affixed at the ends of the base of the laser printer using adhesive tape to prevent tearing, and then was cut with a single pass of the laser beam. The µPAD (Figure SI1), consists of three areas prepared individually and assembled together: (A) the sampling area, (B) the transport channel where 20 µL of phosphate buffer 10 mM pH 7.4 was added, and (C) the detection area where the mineralization was carried out and the recognition of nitrite took place. The µPADs were washed twice by using MilliQ water and ethanol (1:1) for 2 minutes with shaking in order to remove the generated ashes after cutting the paper with the CO_2 laser. Next, the µPADs were dried at room temperature and keeping in a desiccator until its use.

Biomimetic mineralization of detection area of the µPAD in the presence of terbium ions

The mineralization of the detection area of the µPAD, consisting in a cellulose disk, was carried out on a 24-well microtiter plate through three different methods: one of them was based on the ex-situ synthesis of terbium-doped amorphous calcium phosphate (Tb-ACP) nanoparticles and their drop over cellulose disks and the two other methods were based on the in-situ mineralization of the paper. Respect to the former (ex-situ method), terbium doped amorphous calcium phosphate nanoparticles (Tb-ACP) were synthesized through a batch precipitation method, similar to the previously reported synthesis of europium doped ACP.[25] Briefly, two solutions, (A) 50 mL of an aqueous phosphate solution (15 mM K_2HPO_4, pH=12 adjusted with KOH) and (B) 50 mL of an aqueous solution containing 25 mM $CaCl_2$, 25 mM $K_3(C_6H_5O_7)$ and 1.25 mM $Tb(NO_3)_3$ were mixed for 5 minutes under agitation. Then, the precipitates were collected and washed twice with Milli-Q water by centrifugation (5000 rpm, 10 min). Ex-situ mineralization of cellulose was carried out by deposing 100 µL of Tb-ACP solution onto cellulose disks and left to air dry.

The in-situ mineralization of cellulose disks was carried out by incubating in 1 mL of solution A for 10 minutes. Then, 1 mL of solution B was added to trigger to Tb-ACP precipitation in the paper. After 1 hour of incubation under orbital shaking (200 rpm) at room temperature, the mineralizing solution was removed, and the disks were washed twice with Milli-Q water by addition of 1 mL of ultrapure water and incubation for 5 minutes. Finally, the samples were left to air dry. This protocol was optimized to favour the mineral infiltration in the whole volume of cellulose disk. To this aim, cellulose paper was incubated in 1 mL of solution A for 1 hour under orbital shaking (200 rpm) at room temperature. Then, the phosphate solution was removed, and 1 mL of solution B was added to each well. After 1 hour of incubation, the calcium solution was removed. This process was repeated five times. Then, the mineralized cellulose disks were washed and air dried, as previously described.

Physicochemical characterization of mineralized µPAD

Mineralized cellulose fibres were imaged with a field emission scanning electron microscopy (FESEM, GEMINI CARL ZEISS) from Centre for Scientific Instrumentation of the University of Granada (CIC-UGR). The compositional analysis (Ca, P and Tb) was acquired with an Oxford energy dispersed spectroscopy (EDS) detector. The samples were mounted on aluminium stubs using a carbon tape and sputtered with a thin carbon film (BAL-TEC MED-020, CIC-UGR).

The surface of pristine and mineralized cellulose has been analysed by X-ray photoelectron spectroscopy (XPS) to determine its composition. XPS spectra were acquired on a Physical Electronics PHI

VersaProbe II spectrometer (Chanhassen, MN, USA) using monochromatic Al-Kα radiation (47.8 W, 15 kV, and 1486.6 eV) and a beam diameter of 200 µm. The high resolution XPS spectra were recorded with a constant pass energy value at 29.35 eV.

Thermogravimetric analysis was performed using a Mettler–Toledo TGA/DSC1 thermal balance (Mettler-Toledo International Inc., from CIC-UGR) with a heating rate of 10 °C/min up to 950 °C in nitrogen flow. The residue was analysed by using X-ray powder diffraction (XRPD) with a Bruker D8 Advance diffractometer (from CIC-UGR) using Cu Kα radiation (λ = 1.5406 Å), from 15° to 55° (2θ) with a scan rate of 40 s step^{-1}, step size of 0.02° with a HV generator set at 50 kV and 1 mA.

Luminescence measurements

Emission spectra was recorded on a Varian Cary Eclipse fluorescence spectrophotometer (Palo Alto, CA, USA) with double monochromator, a continuous emission xenon light source between 190 and 900 nm and two fixed-width slits and selectable filters. Luminescence intensity was measured using the following conditions: λ_{ex} = 370 nm and λ_{em} = 546 nm, gate time (t_g) 5 ms, delay time (t_d) 0.2 ms, photomultiplier voltage 900 V and excitation and emission slits 5nm. The luminescence intensity at 546 nm of mineralized cellulose was evaluated upon storage time to evaluate the stability of the emission up to 6 months. All experiments were performed using a solid sample holder for luminescent measurements from Agilent Cary Eclipse.

Nitrite detection in designed µPAD

The determination of nitrite was performed by drop casting of 25 µL of different standard solution of nitrite (2-500 µM) onto the sampling area of the µPAD. During the assay, the µPAD was kept in horizontal position and over a non-absorbent surface. The sample moves by capillarity forces through the transport channel to the detection area consisting in the optimized in situ mineralized cellulose disks. After drying (20 minutes), the emission intensity was measured at 546 nm under the excitation of 370 nm. The luminescence intensity of the mineralized paper disk before (I_0) and after adding a nitrite sample (I) was linearized using the Stern-Volmer (S-V) equation:[28]

$$I_0/I = 1 + K_{SV}[C] \qquad \text{(Equation 1)}$$

where K_{SV} is the effective quenching constant (M^{-1}) and [C] is the nitrite concentration (M).

The quenching rate constant (k_q) can be calculated using equation 2 where K_{SV} is the quenching constant (M^{-1}), and τ_0 is the luminescence lifetime (s^{-1}) of mineralized µPAD before the addition of the quencher.

$$k_q = K_{SV}/\tau_0 \qquad \text{(Equation 2)}$$

Time-resolved measurements to evaluate the luminescence lifetimes(τ) were carried out with the following conditions: λ_{ex}=370 nm; λ_{em}=546 nm; t_g=100 µs; t_d=100 µs, the photomultiplier voltage was set at 650 V and the slits widths at 10 nm.

Determination of nitrite in tap water

Nitrite was added to tap water from two different cities in Spain (Zaragoza and Granada) at a final concentration of 10 and 200 µM. Then, 25 µL of the sample was deposited on sampling area of the µPAD and after 20 minutes, the luminescence intensity was measured as previously described.

RESULTS AND DISCUSSION

Optimization of µPAD mineralization in the presence of terbium ions

The first approach to obtain luminescent µPAD was based on the ex-situ synthesis of terbium-doped amorphous calcium phosphate nanoparticles (Tb-ACP) and its dripping onto the detection area consisting of cellulose fibres. The resulting mineral distribution was analysed by scanning electron microscopy in backscattering mode (SEM-BSE) that show high sensitivity to the differences in atomic number appearing in brighter the mineral phase. SEM-BSE image of ex-situ mineralized cellulose disks (Figure 1A) reveals a brighter arc as a part of a ring-like fashion. This phenomenon is known as the coffee ring effect.[29] During the evaporation of a colloidal droplet on a solid surface, drop edges become pinned to the substrate, and capillary flow outward from the centre of the drop brings suspended nanoparticles to the edge as evaporation proceeds, leading to highly concentrated along the original drop edge.[30] Inner areas of the drops showed some mineral deposits (white arrows in Figure 1A) whereas outer zones remained uncovered by the mineral phase (Figure 1A). Taking a closer look at the inner drop area (Figure 1B-C), it can be seen the typical surface morphology of naked cellulose fibres (Figure SI2) and the presence of some isolated mineral aggregates superficially deposited on the fibres of the matrix. SEM-BSE images of the transversal section (Figure 2A-B) show pristine cellulose fibres and the presence of some brighter spots that can be associated to the mineral of the outer layer trapped during the cutting of the transversal section. This finding confirmed the null mineral infiltration into the cellulose disk and thus indicated that ex-situ mineral precipitation and its further dripping into cellulose paper is not a suitable strategy to obtain a homogeneous hybrid material. To overcome this issue, in situ mineralization of cellulose disk was carried out by promoting terbium doped calcium phosphate precipitation in the cellulose fibres through two different approaches: a) one-step protocol based on the incubation of cellulose into a phosphate solution and the further addition of a calcium solution and b) multiple-steps protocol consisting in the incubation of cellulose in phosphate, the removal of this solution and then, its incubation into calcium solution, repeating the protocol several times (see section 2.3).

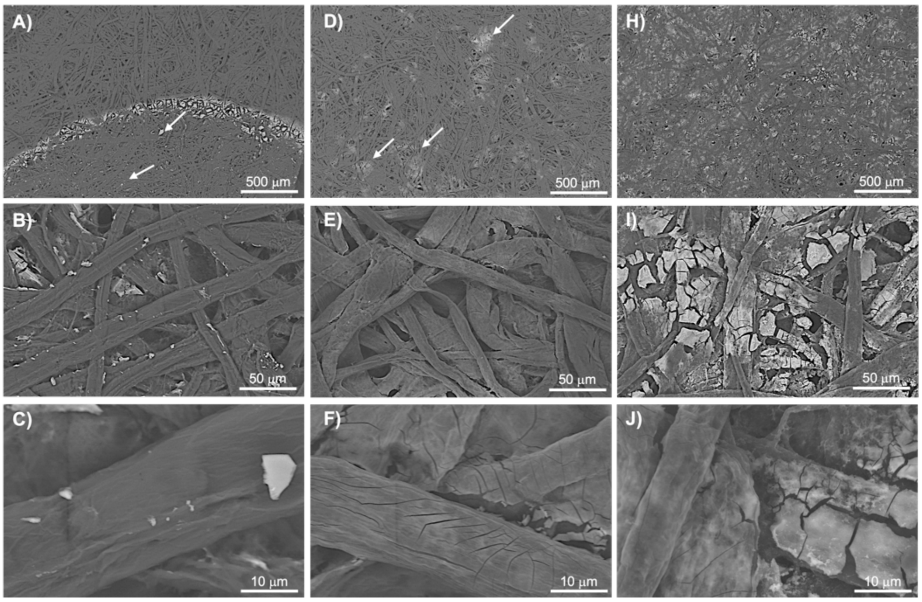

Figure 1. Scanning electron microscopy images in backscattering mode (SEM-BSE) of mineralized cellulose disk through: (A-C) ex-situ Tb-ACP precipitation; (D-F) in-situ mineralization in one-step; and (H-J) optimized in-situ mineralization in multiple-steps.

Both in-situ mineralization methodologies provided a more homogeneous mineral distribution into the cellulose network than ex-situ protocol (Figure 1D,H). Whereas one-step approach prompted to a low extent of the mineralization appearing some brighter areas and poor mineralized fibres (Figure 1D-F), multiple-step mineralization protocol provided a full mineralized cellulose disk (Figure 1H-J). The infiltration of the mineral in the cellulose matrix was also evaluated by SEM-BSE images of the transversal section. While one-step mineralization protocol prompted to naked cellulose fibre and almost null mineral infiltration (Figure 2C-D), the multiple-steps protocol promoted the mineralization of cellulose fibres inside the matrix, as pointed by the white arrows indicating the presence of mineral embedded between the cellulose fibres (Figure 2E-F). These observations suggest that low mineral infiltration during one step mineralization protocol can be associated to the spontaneous precipitation of the mineral phase at the surface of the cellulose disk, forming a mineral layer that hinders calcium ions infiltration and the precipitation of calcium phosphate within cellulose matrix. Through multi-step protocol, we firstly favour cellulose functionalization with phosphate ions during incubation for 1 hour and then we removed phosphate ions to avoid the uncontrolled mineral formation. The further calcium ion addition induced the controlled calcium phosphate nucleation and growth at the phosphate functionalized cellulose fibres providing a better incorporation of the mineral throughout the volume and across the surface of the cellulose matrix, vastly improving the homogeneity of cellulose disk. The role of the organic matrix and ionic precursor concentrations on controlling the nucleation, growth, structure and orientation of the

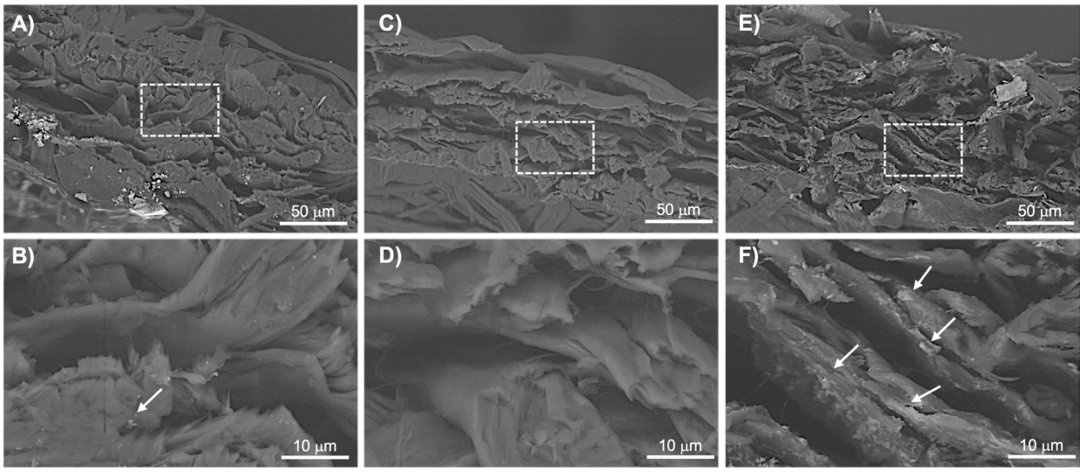

Figure 2. SEM-BSE images of the transversal section of mineralized cellulose disk through: (A-B) ex-situ Tb-ACP precipitation; (C-D) in-situ mineralization in one-step; and (E-F) optimized in-situ mineralization in multiple-steps. Figure 2. SEM-BSE images of the transversal section of mineralized cellulose disk through: (A-B) ex-situ Tb-ACP precipitation; (C-D) in-situ mineralization in one-step; and (E-F) optimized in-situ mineralization in multiple-steps.

mineral within the organic matrix has been previously demonstrated in several systems such as collagen and aromatic short-peptides mineralization.[16,27,31] Thus, this nanostructured hybrid material developed through multi-step mineralization protocol was selected for further physic-chemical characterization and for the evaluation of the luminescent properties towards nitrite quantification.

The high resolution SEM image of optimized material (Figure SI3) revealed the presence of mineral aggregates composed of round shape nanoparticles with the typical morphology of amorphous calcium phosphate (ACP).[32] The Energy dispersive X-ray spectroscopy (EDS) elemental maps (Figure SI4) of the mineralized cellulose surface corroborates that calcium (red), phosphorus (blue) and terbium (green) are evenly distributed across the surface, confirming the formation of terbium doped calcium phosphate during the mineralization protocol. These elements were distributed widely throughout the whole volume of the disk, as shown EDS maps of transversal section (Figure 3). From these results, we can verify that in situ mineralization of cellulose through multi-step protocol leads to homogeneous precipitation of terbium-doped amorphous calcium phosphate nanoparticles within the cellulose matrix.

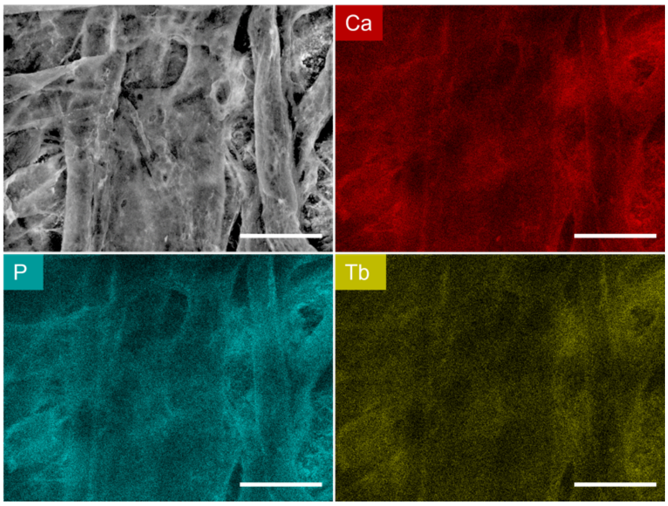

Figure 3. SEM image and Energy dispersive X-ray spectroscopy (EDS) elemental maps of the transversal section of in-situ mineralized cellulose showing the spatial distribution Ca (red), P (blue) and Tb (yellow) of the mineral phase. Scale bar = 100 µm.

The chemical composition of this nanostructured hybrid material was further characterized by X-ray photoelectron spectroscopy (XPS), thermogravimetric analysis (TGA) and X-ray diffraction (XRD) of the ash from TGA. The survey XPS spectra of pristine and mineralized cellulose (Figure 4A) display two relevant peaks at 283.0 and 528.8 eV related to C 1s and O 1s, respectively. The deconvoluted high-resolution C 1 s spectrum (Figure 4B) of pristine cellulose shows three main peaks: one major peak at 286.2 eV corresponding to C–O bond; a peak at 284.7 eV corresponding to C–C bonds, and a third one around 287.4 eV that corresponds to O–C–O bond.[33] In the case of mineralized cellulose (Figure 4C), a clear asymmetry in the C1s energy region could be due to the presence of carboxylic groups (-COOH) from citrate, a molecule widely used in bioinspired mineralization due to its key dual role in the calcium phosphate crystallization.[26,34,35] Citrate stabilizes the amorphous calcium phosphate precursor and controls the size of apatite nanocrystals by the non-classical oriented aggregation mechanism.[26,34,35] While the deconvoluted high-resolution O 1 s spectrum of pristine cellulose (Figure 4D) only displays a peak at 532.6 eV corresponding with C-OH/C-O-C bond, it shows an addition peak at 531.0 eV ascribed to O-P-O bond of phosphate group of the mineral in the case of mineralized cellulose (Figure 4E).[36]

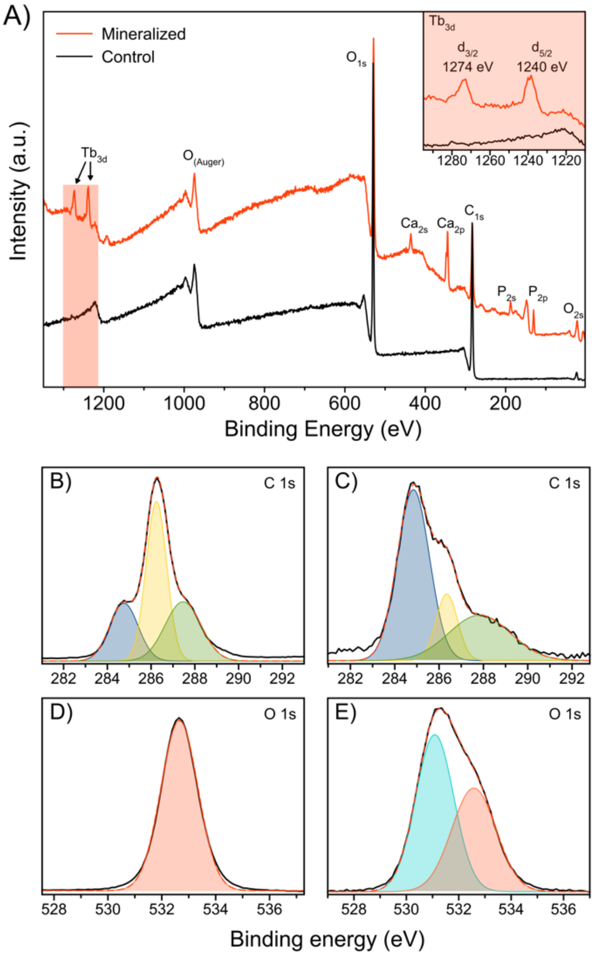

Figure 4. A) The XPS survey spectra of pristine (control) and mineralized cellulose disk of the µPAD. The inset shows the Tb 3d region of mineralized cellulose. (B and C) The C 1 s spectrum of pristine and mineralized cellulose disk, respectively. (D and E) The O 1 s spectrum of pristine and mineralized cellulose disk, respectively. Black dots display the experimental data whereas red dashed line represents the fitting data by sum up the contribution of the curves related to the binding energy of the respective bonds.

The XPS spectra of mineralized cellulose also displays the characteristic peaks of Ca 2p and Ca 2s, P 2p and P 2s and Tb 3d ascribed to Tb-ACP nanoparticles.[24] The Tb 3d spectrum (inset figure 4A) shows two peaks at 1242.0 eV and 1274.0 eV corresponding to the $3d_{5/2}$ and $3d_{3/2}$ spin-orbit doublets of Tb^{3+}.[24] The atomic concentration of mineralized cellulose (Table SI1) calculated by XPS revealed a 6.06% P, 5.57% Ca and 0.86% Tb. The mineral content was also quantified by thermogravimetric analysis. TGA curves (Figure SI5A) mainly display two weight loss: the first loss from 20 ºC to 150 ºC due to the adsorbed and bound water and the second loss at 341ºC due to the degradation of cellulose including depolymerization, dehydration, and decomposition of glucosyl units followed by the formation of a charred residue.[37] The mineralization of cellulose hampered its thermal degradation by increasing the onset temperature up to 362ºC (inset Figure SI5A). This finding highlights the strong interaction between the cellulose and Tb-ACP nanoparticles, leading to an enhancement of the thermostability of the cellulose. Whereas the resultant residue of the pristine cellulose (control) after 650ºC was close to 10 wt.%, mineralized cellulose presented a residue around 19%, which means a Tb-ACP content of 9 wt.%. X-ray diffraction pattern of this residue (Figure SI5B) shows the characteristic reflections of hydroxyapatite (HA, ASTM card file No: 09-432) due to ACP conversion into HA during thermal treatment.[26] This result along with round shape nanoparticle morphology observed by SEM and Ca, P, Tb distribution in EDS maps confirmed the formation of Tb-ACP nanoparticles in cellulose matrix.

3.2. Luminescent properties of mineralized µPAD

The emission spectrum of the mineralized µPAD is displayed in Figure 5A. It exhibits the characteristic luminescence of Tb^{3+} ions excited at 370 nm in the wavelength range of 450 nm and 650 nm.[38] The most intense peak at 546 nm corresponded to the $^5D_4 \rightarrow {}^7F_5$ transition, while the other peaks at 491, 586 and 622 nm corresponded to the $^5D_4 \rightarrow {}^7F_6$, $^5D_4 \rightarrow {}^7F_4$ and $^5D_4 \rightarrow {}^7F_3$ transitions, respectively. Very few studies reported on the assessment of the storage stability of developed µPADs, which is crucial for the widespread adoption of these devices for different applications such as the chemical analysis of water.[1,10] A recent study demonstrated the stability of µPADs up to 60 days but in vacuum and at 4ºC.[10] We monitored the temporal evolution of emission intensity at 546 nm of mineralized µPAD up to 6 months (Figure 5B). The normalised intensity remained constant even after 6 months of storage under the darkness and at room temperature. Thus, biomimetic mineralization of µPAD is a promising strategy to develop luminescent sensors that overcome the low photochemical stability of organic fluorescent dyes, quantum dots or organosilica nanodots.[11] The effect of the pH on luminescent signal was also evaluated (Figure SI6). The normalised intensity graph in the pH range of 2-12 rules out any influence of the pH on the emission intensity.

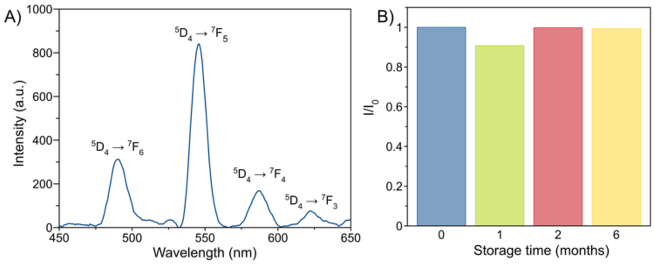

Figure 5. A) Emission (λ_{exc} =370 nm) spectrum of mineralized µPAD. B) Normalized luminescence response of mineralized µPAD respect to the storage time. I_0 and I refer to the intensity of the emission peak at 546 nm measured just after preparation and at specific times, respectively.

3.3. Analytical performance of the designed µPAD for nitrite quantification

The sensitivity of the designed µPAD with respect to nitrite was evaluated by luminescence spectroscopy. The figure 6A shows the emission spectra of the µPAD under excitation at 370 nm before and after adding a 400 µM nitrite aqueous solution. The strong green emission of Tb^{3+} ions were quenched upon addition of nitrite solution (Figure 6A). The concentration-responsive quenching of the emission (Figure 6B) follows a good linear correlation (R^2 = 0.989) in the range of 10-400 µM, adjusting the data set to Stern-Volmer equation (equation 1) with a quenching constant (K_{sv}) of $2.38 \cdot 10^{-3}$ μM^{-1} (Table 1).

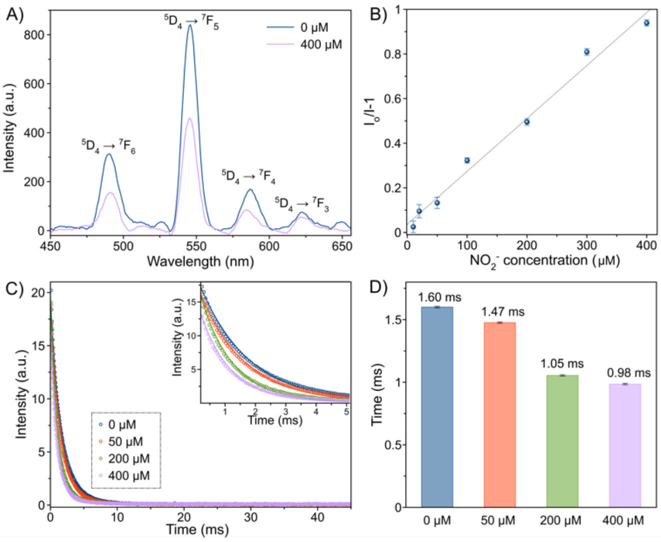

Figure 6. A) Emission spectra of the designed µPAD before (0 µM) and after adding 25 µL of a nitrite aqueous solution (400 µM). B) The linear relationship (dotted line) between $I_0/I-1$ and nitrite ion concentration. I_0 and I are the intensity in the absence and presence of increasing nitrite concentrations, respectively. The experimental data (circles) represent the mean average and the error bars correspond to S.E.M (n=3). C) Luminescence decay curves of designed µPAD before (0 µM) and after adding increasing concentrations of nitrite (50, 200 and 400 µM). The symbols represent the experimental data and lines represent the corresponding fitting to a single exponential equation: $I = A1 \exp\{-t/\tau\} + A2$. D) The estimated lifetime (τ) of the emission for each condition. Error bars correspond to S.E.M (n=3).

The relevant analytical parameters of this sensing material are summarized in Table 1. The limits of detection (LOD) and quantification (LOQ) for nitrite were 10 and 33 µM, respectively, as determined in accordance with the standard criteria.[39] Both parameters are below the maximum contaminant level of nitrite ions in 3 ppm (65 µM) in drinking water established by the World Health Organization (WHO).[7,5] Moreover, the LOD of this nitrite sensor is similar to a previously published study that revealed LOD values between 6.8 to 8.1 µM for terbium-based luminescent cellulose hydrogels.[40] Measurement reproducibility was evaluated at two different nitrite concentrations, *i.e.,* 10 and 200 µM, and revealed good coefficients of variation (2.6% and 1.2%, respectively).

Table 1. Analytical characteristics of designed µPAD for nitrite determination.

Analytical parameter	Value
Measurement range (µM)	10-400
Equation	y = a + b*x
R^2	0.986
Slope (μM^{-1})	0.002 ± 1.03E-4
Intercept (a.u.)	0.06 ± 0.02
LOD (µM)	10
LOQ (µM)	33
Precision 10 µM (%)	2.6
Precision 200 µM (%)	1.2

a.u.: arbitrary units

To figure out the quenching behaviour towards nitrite ions, the sensing mechanism was investigated. The luminescence lifetimes (τ_o) of designed µPAD was 1.6 ms (Figure 6C-D), which is in agreement with previously reported values for Tb-doped nanoapatite.[24,41] The lifetimes decreased with the increase in nitrite concentration (Figure 6C-D), indicating a dynamic quenching originated from the interaction between nitrite ions and Tb-ACP nanoparticles of designed µPAD, causing faster exciton decays and shorter luminescence lifetimes.[24] Previous studies pointed out an energy transfer from Tb^{3+} to nitrite ions after their coordination interaction owing to the slightly higher T_1 energy of NO_2^- (19,084 cm^{-1}) than the $^5D_4$ energy level of Tb^{3+} (20,500 cm^{-1}).[42,43] In addition, the UV-Vis spectrum of the sodium nitrite (Figure SI7) did not show absorption band at the excitation wavelength (λ_{exc} =370 nm) , which excludes the possibility of the competitive absorption mechanism.

We evaluated the selectivity of the designed µPAD by measuring the emission spectra in the individual presence of different interfering species commonly found in water (Figure SI8A). Whereas most of the species did not elicit any discernible effect, cationic ions (*i.e.,* Fe^{3+}, Cu^{2+} and Mg^{2+}) caused a decrease of the luminescent intensity, being this effect more noticeable for copper ions. The interference of these ions can be eliminated by adding EDTA solution in the microfluidic channel. EDTA can complex these cationic ions[44,45] before arriving to the detection area, almost eliminating its interference in the emission signal, as shown in the case of copper ions (Figure SI8B), the strongest interfering specie. We also carried out a recovery experiment by spiking with 10 and 200 µM of standard nitrite in tap water with values ranging from 95.2% to 104.5% (Table SI2). These good recovery percentages confirmed the suitability of mineralized µPAD for nitrite detection in water samples with relatively good accuracy and reproducibility.

Conclusions

In summary, we optimized an in-situ biomimetic mineralization of µPAD towards the design of a potentially powerful analytical platform for the monitoring of water pollutants. SEM, XPS, TGA and XRD analysis confirmed the strong interaction between the cellulose and precipitated Tb-ACP nanoparticles, leading to a better incorporation of the mineral both throughout the volume and across the surface of the cellulose disks. This approach provided luminescent µPAD with long-term emission stability (up to 6 months in storage) and excellent sensitivity towards nitrite ions, being the LOD below the permissible limits of nitrite in drinking water. The decrease of the lifetime with the increase in nitrite concentration revealed a dynamic quenching due to the interaction between nitrite ions and Tb-ACP nanoparticles of designed µPAD. Recovery analysis in tap water confirmed that the µPAD is suitable for nitrite detection in real samples with good accuracy and reproducibility. Our findings indicated that the biomimetic mineralization of cellulose µPAD in presence of lanthanide ions is a promising environmentally friendly strategy to design potential luminescence sensors for water monitoring applications.

Author Contributions

We strongly encourage authors to include author contributions and recommend using CRediT for standardised contribution descriptions. Please refer to our general author guidelines for more information about authorship.

The manuscript was written through contributions of all authors. All authors have given approval to the final version of the manuscript.

Conflicts of interest

“There are no conflicts to declare”.

Acknowledgements

This work has been performed thanks to the funding from the FEDER/Ministerio de Ciencia, Innovación, Universidades-Agencia Estatal de Investigación (MCIN/AEI/ 10.13039/501100011033) and “ESF Investing in your future”, through the projects flexihealth (PID2020-117344RB-I00), nanoSOP (PDC2022-133191), nanobip (TED2021-132151A-I00) and RYC2021-032734-I. This study was also supported by the project P21-00386 funded by FEDER/Junta de Andalucía-Consejería de Transformación Económica, Industria, Conocimiento y Universidades (Spain).

References

1 M. I. G. S. Almeida, B. M. Jayawardane, S. D. Kolev and I. D. McKelvie, *Talanta*, 2018, **177**, 176–190.

2 S. Finance, 2021.

3 European Commission, https://environment.ec.europa.eu/topics/water/nitrates_en.

4 R. Picetti, M. Deeney, S. Pastorino, M. R. Miller, A. Shah, D. A. Leon, A. D. Dangour and R. Green, *Environ Res*, 2022, **210**, 112988.

5 N. S. Bryan, D. D. Alexander, J. R. Coughlin, A. L. Milkowski and P. Boffetta, *Food and Chemical Toxicology*, 2012, **50**, 3646–3665.

6 L. B. Maia and J. J. G. Moura, *Chem Rev*, 2014, **114**, 97.

7 J. A. Cotruvo, *Journal-American Water Works Association*, 2017, **109**, 44–51.

8 P. Singh, M. K. Singh, Y. R. Beg and G. R. Nishad, *Talanta*, 2019, **191**, 364–381.

9 L. Walekar, T. Dutta, P. Kumar, Y. S. Ok, S. Pawar, A. Deep and K. H. Kim, *TrAC - Trends in Analytical Chemistry*, 2017, **97**, 458–467.

10 F. T. S. M. Ferreira, R. B. R. Mesquita and A. O. S. S. Rangel, *Talanta*, 2020, **219**, 121183.

11 X. Yue, Z. Zhou, Y. Wu, M. Jie, Y. Li, H. Guo and Y. Bai, *New Journal of Chemistry*, 2020, **44**, 8503–8511.

12 F. Nudelman and N. A. J. M. Sommerdijk, *Angewandte Chemie International Edition*, 2012, **51**, 6582–6596.

13 U. G. K. Wegst, H. Bai, E. Saiz, A. P. Tomsia and R. O. Ritchie, *Nat Mater*, 2014, **14**, 23.

14 A. L. Boskey, *J Cell Biochem Suppl*, 1998, **30–31**, 83–91.

15 G. Ramírez Rodríguez, T. Patrício and J. Delgado López, *Natural polymers for bone repair*, Elsevier Ltd, Second Edi., 2019.

16 Y. Wang, T. Azaïs, M. Robin, A. Vallée, C. Catania, P. Legriel, G. Pehau-Arnaudet, F. Babonneau, M.-M. Giraud-Guille and N. Nassif, *Nat Mater*, 2012, **11**, 724–733.

17 A. Salama, *Int J Biol Macromol*, 2019, **127**, 606–617.

18 V. N. Narwade, R. S. Khairnar and V. Kokol, *J Polym Environ*, 2018, **26**, 2130–2141.

19 Y. Jin, Y. Ni, M. Pudukudy, H. Zhang, H. Wang, Q. Jia and S. Shan, *Mater Chem Phys*, 2022, **275**, 125135.

20 D. Núñez, R. Cáceres, W. Ide, K. Varaprasad and P. Oyarzún, *Int J Biol Macromol*, 2020, **165**, 2711–2720.

21 I. A. Neacsu, A. E. Stoica, B. S. Vasile and E. Andronescu, *Nanomaterials*, 2019, **9**, 239.

22 C. Qi, J. Lin, L.-H. Fu and P. Huang, *Chemical Society Reviews*, 2018, **47**, 357–403.

23 R. L. Yang, Y. J. Zhu, F. F. Chen, L. Y. Dong and Z. C. Xiong, *ACS Applied Materials and Interfaces*, 2017, **9**, 25455–25464.

24 H. Liu, X. Wang, T. Abeywickrama, F. Jahanbazi, Z. Min, Z. Lee, J. Terry and Y. Mao, *Environmental Science: Nano*, 2021, **8**, 3711–3721.

25 I. Ortiz-Gómez, G. B. Ramírez-Rodríguez, L. F. Capitán-Vallvey, A. Salinas-Castillo and J. M. Delgado-López, *Colloids and Surfaces B: Biointerfaces*, , DOI:10.1016/j.colsurfb.2020.111337.

26 J. M. Delgado-López, M. Iafisco, I. Rodríguez, A. Tampieri, M. Prat and J. Gómez-Morales, *Acta Biomaterialia*, 2012, **8**, 3491–3499.

27 J. M. Delgado-López, F. Bertolotti, J. Lyngsø, J. S. Pedersen, A. Cervellino, N. Masciocchi and A. Guagliardi, *Acta Biomaterialia*.

28 O. Stern and M. Volmer, *Phys. Z*, 1919, **20**, 183–188.

29 P. J. Yunker, T. Still, M. A. Lohr and A. G. Yodh, *nature*, 2011, **476**, 308–311.

30 P. J. Yunker, T. Still, M. A. Lohr and A. G. Yodh, *nature*, 2011, **476**, 308–311.

31 M. C. Mañas-Torres, G. B. Ramírez-Rodríguez, J. I. Garcia-Peiro, B. Parra-Torrejón, J. M. Cuerva, M. T. Lopez-Lopez, L. Alvarez de Cienfuegos and J. M. Delgado-López, *Inorganic Chemistry Frontiers*, , DOI:10.1039/d1qi01249e.

32 C. Combes and C. Rey, *Acta Biomaterialia*, 2010, **6**, 3362–3378.

33 A. Alanis, J. H. Valdés, N. V. María Guadalupe, R. Lopez, R. Mendoza, A. P. Mathew, R. Díaz De León and L. Valencia, *RSC Advances*, 2019, **9**, 17417–17424.

34 M. Iafisco, G. B. Ramírez-Rodríguez, Y. Sakhno, A. Tampieri, G. Martra, J. Gómez-Morales and J. M. Delgado-López, *CrystEngComm*, 2015, **17**, 507–511.

35 Y. Y. Hu, A. Rawal and K. Schmidt-Rohr, *Proceedings of the National Academy of Sciences of the United States of America*, 2010, **107**, 22425–22429.

36 L. Zha, Y. Zheng, J. Che and Y. Xiao, *New Journal of Chemistry*, 2021, **45**, 22354–22360.

37 H. Yang, R. Yan, T. Chin, D. T. Liang, H. Chen and C. Zheng, *Energy & fuels*, 2004, **18**, 1814–1821.

38 F. S. Richardson, *Chemical Reviews*, 1982, **82**, 541–552.

39 J. N. Miller and J. C. Miller, *Estadística y quimiometría para química analítica*, 2002.

40 Z. Zhou and Q. Wang, *Sensors and Actuators, B: Chemical*, 2012, **173**, 833–838.

41 J. Gómez-Morales, R. Fernández-Penas, F. J. Acebedo-Martínez, I. Romero-Castillo, C. Verdugo-Escamilla, D. Choquesillo-Lazarte, L. D. Esposti, Y. Jiménez-Martínez, J. F. Fernández-Sánchez and M. Iafisco, *Nanomaterials*, 2022, **12**, 1257.

42 F. Tanaka, T. Ishibashi and M. Okamoto, *Journal of Photochemistry and Photobiology A: Chemistry*, 1993, **74**, 15–19.

43 H. Min, Z. Han, M. Wang, Y. Li, T. Zhou, W. Shi and P. Cheng, *Inorganic Chemistry Frontiers*, 2020, **7**, 3379–3385.

44 I. Ortiz-Gomez, M. Ortega-Muñoz, A. Salinas-Castillo, J. A. Álvarez-Bermejo, M. Ariza-Avidad, I. de Orbe-Payá, F. Santoyo-Gonzalez and L. F. Capitan-Vallvey, *Talanta*, 2016, **160**, 721–728.

45 S. Sarkar, M. Chatti, V. N. K. B. Adusumalli and V. Mahalingam, *ACS Applied Materials and Interfaces*, 2015, **7**, 25702–25708.

1 Citations should appear here in the format A. Name, B. Name and C. Name, *Journal Title*, 2000, **35**, 3523; A. Name, B. Name and C. Name, *Journal Title*, 2000, **35**, 3523.

2 …

Formatting – please delete this box prior to submission

- Our template aims to give you an idea of what your article will look like, however the final version will be formatted in our house style and may look different.
- Please consult the Styles menu for recommended formatting for all text, including footnotes, references, tables, images and captions.
- Text should not be wrapped around graphics.

During production:

- Graphics, including tables, will be located at the top or bottom of the column following their first citation in the text. Graphics can be single column or double column as appropriate and require captions.
- Equations will be placed in the flow of the text.
- Sufficient space will be inserted around graphics for clarity of reading; a horizontal bar will also be used to separate all inserted graphics, tables and their captions from the text.

If you are experiencing difficulty using our template, please consult our 'Using the Template' guide, found here.

We encourage the citation of primary research over review articles, where appropriate, in order to give credit to those who first reported a finding. Find out more about our commitments to the principles of San Francisco Declaration on Research Assessment (DORA).